Microscopic Insights into Long-Range 1D Ordering in a Dense Semi-Disordered Molecular Overlayer

Ryan T. Hannagan[‡,a], Isaac Onyango[‡,b], Amanda Larson, Jean-Sabin McEwen[★,b,c,d,e,f], E. Charles H. Sykes[★,a]

‡ These authors contributed equally to the work

[a] Department of Chemistry, Tufts University, Medford, MA 02155, USA

[b] The Gene and Linda Voiland School of Chemical Engineering and Bioengineering, Washington State University, Pullman, WA 99164, USA

[c] Department of Chemistry, Washington State University, Pullman, WA 99164, USA

[d] Department of Physics, Washington State University, Pullman, WA 99164, USA

[e] Department of Biological Systems Engineering, Washington State University, Pullman, WA 99164, USA

[f] Institute of Integrated Catalysis, Pacific Northwest National Laboratory, Richland, WA 99354, USA

★Corresponding authors: J.-S. McEwen (js.mcewen@wsu.edu) and E. C. H. Sykes (Charles.Sykes@tufts.edu).

Experimental Methods

All experimental work was conducted in two separate ultra-high vacuum (UHV) chambers. The first is a low temperature scanning tunneling microscope (LT-STM) chamber (Omicron Nanotechnology) comprised of a STM chamber (base pressure $<1 \times 10^{-11}$ mbar) attached to a preparation chamber (base pressure $<2 \times 10^{-10}$ mbar). All imaging was done at 5 K after a brief anneal to between ~40 and ~80 K to equilibrate the molecules. Typical imaging conditions involved biases of 60 or -60 mV and tunneling currents <70 pA. The second UHV chamber is a temperature programed desorption (TPD) chamber (base pressure $<1 \times 10^{-10}$ mbar) equipped with a mass spectrometer (Hiden Hal RC 201) and an infrared spectrometer (Bruker Tensor II). The mass spectrometer is mounted on a z-drive and capable of being advanced to within 1 mm of the sample surface for TPD measurements. All TPD experiments were conducted with a linear heating rate of 1.5 K/s. The crystal was cooled via liquid nitrogen and heated resistively. Temperatures were measured using a K-type thermocouple welded to the back of the crystal. For infrared (IR) experiments, a beam was generated outside of UHV and directed into the chamber with a series of gold-plated mirrors. After reflection off the Cu(111) sample at a grazing angle, the beam was collected with another series of gold mirrors and directed into a MCT (mercury cadmium tellurium) detector. ZnSe windows were used to prevent loss of IR light and the entire non-UHV portion of the set up was enclosed by a dry-air purge box. The IR background (2000 scans) was collected at 90 K on clean Cu(111) followed by propene adsorption and collection of a spectra (2000 scans) with 4 cm^{-1} resolution. To eliminate slight slanting of the spectra, the spectra were background subtracted in OriginPro. Cu(111) crystals (Princeton Scientific) were cleaned by repeated cycles of argon ion bombardment with an RBD sputter gun (~2 µA drain current, 1.5 keV beam energy, 5×10^{-5} mbar Ar) and thermal annealing to ~700 K. Propylene (Matheson Tri-gas, 99.9% purity) desorbed reversibly from the crystal, so cleaning was performed at the start of the week for STM experiments, and at the start of each day for TPD experiments. Dosing was done via prevision leak valve. All propene coverages are given with respect to the saturated monolayer (i.e., the densest phase of propene before multilayer growth) of propene on Cu(111).

Computational Methods

All theoretical calculations were performed using closed-shell Kohn-Sham Density Functional Theory (DFT) implemented in the Vienna *Ab initio* Simulation Package (VASP).[1,2] The projector augmented wave (PAW) method was applied for treatment of core electrons, using the PAW potentials that were released in 2015.[3,4] The generalized gradient approximation in the form of Becke86 (optB86b-vdW) was adopted for the exchange-correlation functional to account for dispersion in the interactions.[5,6] Spin-polarization effects were not taken into account in the calculations since the Cu(111) slab is non-magnetic. The plane-wave basis set all calculations was created using a cutoff energy of 500 eV.

We modelled the experimentally observed propene overlayer structure with a $(3 \times 3\sqrt{3})$rect surface unit cell. Such a model only considers one row of propene molecules since we consider the interaction between the rows to be negligible in the saturated monolayer structure.

The corresponding distance between the propene rows is 1.323 nm in the t-shape and floating configuration models that are shown in Figure 2. In addition, the surface is modeled with a four-layer slab model that has 15 Å of vacuum in between two successive slabs. The bottom two layers of the slab were fixed while the top two were relaxed. The lattice constant for the forementioned bulk positions was computed to be 3.601 Å (experimentally 3.597 Å)[7] using a 20×20×20 Monkhorst-Pack grid. For all surface calculations, a 6×2×1 Monkhorst-Pack grid was employed to sample the first Brillouin zone. A Methfessel-Paxton smearing with a width of 0.1 eV was used, and a convergence criterion was $1×10^{-4}$ eV and 0.03 eV/Å for electronic energies and interatomic forces on the relaxed layers, respectively. The average adsorption energies of propene (PY) ($E_{ads}^{average}(\theta)$) are quantified by:

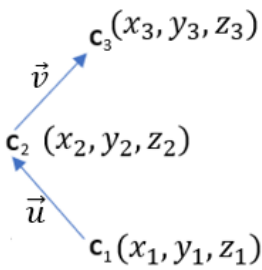$$E_{ads}^{average}(\theta) = \frac{\left(E_{N_{PY}/Cu(111)}(\theta) - \left(E_{Cu(111)} + N_{PY}\,E_{PY(g)}\right)\right)}{N_{PY}} \qquad (1)$$

where $E_{N_{PY}/Cu(111)}(\theta)$ is the total energy of the PY/Cu(111) adsorption system at a coverage of θ, $E_{Cu(111)}$ is the total energy of the clean slab, N_{PY} is the number of adsorbed propene molecules that are adsorbed at a coverage of θ and $E_{PY(g)}$ is the total energy of a propene molecule in the gas phase.

Adsorption Energy and Molecular Tilt of Isolated Propene

The adsorption energy of an isolated propene molecule (Figure S1a) is -0.68 eV, which is 0.28 eV stronger than in a previous study where the optB88-vdW functional and a 2×2×1 Monkhorst-Pack grid was used.[8] This difference in adsorption energy is mainly due to the difference in the Fast Fourier Transform grids used in the respective studies. A PREC=Accurate precision grid is used in this study while a PREC=High precision grid was used in the previous study.

The isolated propene molecule (Figure S1a) adsorbs on the surface with a 19° angle between the plane containing the molecule (the molecular plane) and the plane of surface (the molecular tilt angle). This angle value is in reasonable agreement with those in the literature.[9] The molecular tilt angle was determined by calculating:

$$c_3(x_3, y_3, z_3)$$
$$\vec{v}$$
$$c_2\,(x_2, y_2, z_2)$$
$$\vec{u}$$
$$c_1(x_1, y_1, z_1)$$
$$\vec{v} = [x_3 - x_2, y_3 - y_2, z_3 - z_2]$$
$$\vec{u} = [x_1 - x_2, y_1 - y_2, z_1 - z_2]$$

$$\vec{v} \times \vec{u} = \vec{n_1} \qquad (2)$$

$$\vec{a} \times \vec{b} = \overrightarrow{n_2} \tag{3}$$

$$\theta_d = \cos^{-1}\left(\frac{\overrightarrow{n_1} \cdot \overrightarrow{n_2}}{|\overrightarrow{n_1}||\overrightarrow{n_2}|}\right) \tag{4}$$

where c_1, c_2 and c_3 are the cartesian coordinates of the three carbon atoms of propene. In Equations 2, 3 and 4, $\vec{v}$ and $\vec{u}$ are the vectors defining the molecular plane, $\vec{a}$ and $\vec{b}$ are the $\vec{a}$ and $\vec{b}$ lattice vectors of the surface, $\overrightarrow{n_1}$ is the normal vector to the molecular plane, $\overrightarrow{n_2}$ is the normal vector to plane of the surface and θ_d is the molecular tilt angle. The lattice vectors of the surface were used because the surface is fairly flat.
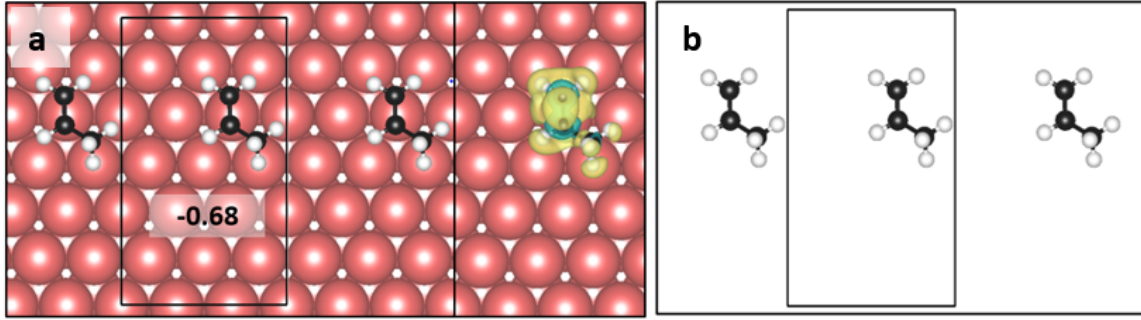

Figure S1: Panel a is the isolated propene molecule adsorbed on the Cu(111) surface (coverage of ~0.056 molecules per Cu atom) with the corresponding adsorption energy in eV and differential charge density simulated at an isosurface level of 0.001 electrons/Bohr³. The yellow and blue areas on the differential charge densities show regions of charge depletion and charge gain, respectively. Panel b is the isolated propene molecule in the absence of Cu(111) surface. The pink, black and white spheres are Cu, C and H atoms, respectively.

Interactions of Propene on Cu(111)

To elucidate the direct (through-space) interaction between the propene molecules, the differential charge densities were simulated for the systems in the absence of the Cu(111) surface, but with the molecules in fixed geometries so their configurations are preserved after removing the surface. This eliminates the possibility of surface-mediated effects. The differential charge densities (Figure S2) shows that there is hardly any interaction between the propene molecules in all the configurations even with the addition of a third propene. The differential charge densities ($\Delta\rho$) were obtained by evaluating:

$$\Delta\rho(\vec{r}) = \rho_{N_{PY}/Cu(111)}(\vec{r}) - \rho_{(N_{PY}-n_{PY})}(\vec{r}) - \rho_{n_{PY}/Cu(111)}(\vec{r}) \tag{5}$$

where $\rho_{N_{PY}/Cu(111)}(\vec{r})$, $\rho_{(N_{PY}-n_{PY})(g)}(\vec{r})$, and $\rho_{n_{PY}/Cu(111)}(\vec{r})$, represent the charge distribution for the adsorbed system (surface with all adsorbates present), $N_{PY} - n_{PY}$ propene molecules in the gas phase, and the clean Cu(111) surface with the remaining n_{PY} pre-adsorbed propene molecules, respectively. Equation 5 above can also be used for differential charge densities in the absence of the surface.
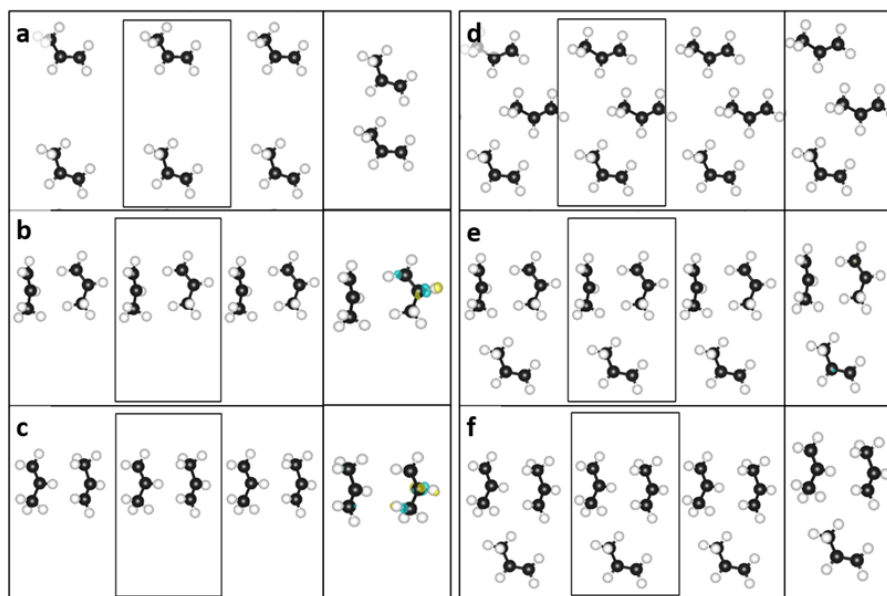
Figure S2: Configurations of propene molecules in absence of Cu(111) surface with their respective differential charge densities simulated at an isosurface level of 0.001 electrons/Bohr³. The geometries of these gas phase propene configurations are constrained at their optimized positions when adsorbed on a Cu(111) surface as depicted in Figure 2. The yellow and blue areas on the differential charge densities show regions of charge depletion and charge gain, respectively. Panels d, e and f are configurations where a third propene molecule was added to the configurations shown in panels a, b and c. Panels b and e show the t-shape configurations and panels c and f show the floating configurations. The black and white spheres are C and H atoms respectively.

To further examine the direct interactions between the propene molecules, we calculated the formation energies for the structures that are depicted in Figure S2. The formation energies are defined as

$$E_{\text{form}}(\theta) = \frac{\left(E_{\text{N}_{\text{PY(g)}}}(\theta) - N_{\text{PY}}E_{\text{PY(g)}}^{\text{isolated}}\right)}{N_{\text{PY}}} \qquad (6)$$

where $E_{\text{N}_{\text{PY(g)}}}(\theta)$ is the total energy of N_{PY} gas phase propene molecules that are constrained at their optimized positions on a Cu(111) surface at a coverage of θ while $E_{\text{PY(g)}}^{\text{isolated}}$ is the total energy of an isolated propene molecule in the gas phase. The formation energies were calculated with respect to two different initial state references of the isolated propene molecule. The first reference uses an unconstrained gas phase propene molecule. The second reference also uses an isolated gas phase propene molecule, but its geometry was constrained to its optimized conformation when it adsorbs on a Cu(111) surface at a coverage of ~0.056 molecules per Cu atom (as depicted in Figure S1). Both initial state references were calculated using the unit cell as depicted in Figure S1. The resulting formation energies were calculated with the optB86b-vdW functional and the RPBE functional and the values are given in Table S1 and Table S2 respectively. We note that a positive formation energy value indicates that the formation of that particular structure is thermodynamically unfavorable.

The through-space interaction energies can be estimated by comparing the value of the adsorption energy difference between the two and three molecule structures (Figure 2e and 2b for the t shape configuration, and Figure 2f and 2c for the floating configuration) to the corresponding formation energy differences using the data from Table S1 and S2 (without the surface). As can be seen from Table S1, the through-space interaction energies between the propene adsorbates are small and one does not see the same stabilization effect as when the surface is present, illustrated in Figure 2. For example, the formation energy difference between the two molecule and three molecule floating configurations (shown in Figure S2 panels c and f) is 0.04 eV using the unconstrained reference (see Table S1) while in the presence of the surface the adsorption energy difference is -0.07 eV (see Figure 2). We arrive at a similar result for the constrained reference. As a result, the interaction between the propene adspecies is surface mediated.

Further, when we use the revised Perdew-Burke-Ernzerhof (RPBE)[10] functional in which dispersion forces are not accounted for, the configurations also generally become less favorable (see formation energies in Table S2). In particular, when taking the unconstrained propene molecule as a reference, configuration f shown in Figure S2 ($E_{form}(\theta) = 0.12$ eV) is less stable as compared to configuration c ($E_{form}(\theta) = 0.09$ eV) using the RPBE functional. We note however that the formation energies of both structures are positive meaning that they are thermodynamically unfavorable, while these structures are thermodynamically stable (i.e. negative formation energies) when using the optB86b-vdW functional (see Table S1). We arrive at a similar conclusion when taking the constrained isolated propene molecule as a reference.

Table S1: Formation energies for the configurations shown in Figure S2. The middle column gives the formation energies using an unconstrained isolated propene molecule in the gas phase as a reference. The right column also uses an isolated gas phase propene molecule as a reference, but its geometry is constrained to its optimized conformation when adsorbed on the Cu(111) surface as depicted in Figure S1. The calculations were performed using the optB86b-vdW functional.

Configuration	Ref: unconstrained propene molecule in gas phase (eV)	Ref: Isolated propene molecule (eV)
a	0.07	-0.07
b	0.03	-0.11
c	-0.07	-0.21
d	-0.01	-0.15
e	0.02	-0.12
f	-0.03	-0.17

Table S2: Formation energies in electron volts for configurations in Figure S2. The middle column gives the formation energies using an isolated unconstrained propene molecule in the gas phase as a reference. The right column also uses an isolated gas phase propene molecule as a reference, but its geometry is constrained to its optimized conformation when adsorbed on the Cu(111) surface as depicted in Figure S1. The calculations here are done using the RPBE functional.

Configuration	Ref: unconstrained propene molecule in gas phase (eV)	Ref: Isolated propene molecule (eV)
a	0.11	-0.03
b	0.15	0.02
c	0.09	-0.05
d	0.07	-0.06
e	0.14	0.00
f	0.12	-0.02

Energetic Insensitivity to the Position of the Third Propene Molecule

Furthermore, we show in Figure S3 the effect of translating the third PY molecule to the left and the right. This barely affects the corresponding adsorption energies. As such, we can consider the placement of the third PY molecule is not sensitive on its position in-between the 1D chains, which is consistent with the experimental observations.
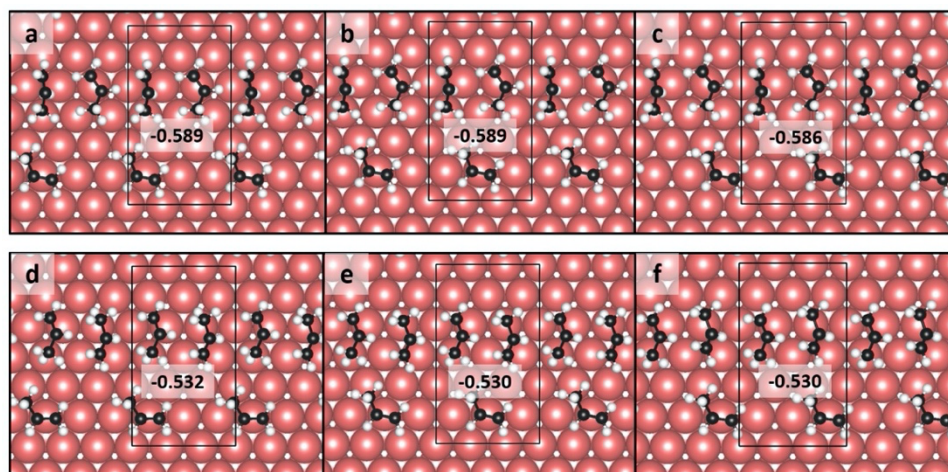

Figure S3: Configurations of propene molecules adsorbed on Cu(111) surface with their respective adsorption energies in eV. Panels a, b and c depict the adsorption position of a third propene molecule adsorbed at different positions relative to the t-shape like configuration, and panels d, e and f depict the adsorption of a third propene molecule adsorbed at different positions relative to the floating configuration. The pink, black and white spheres are Cu, C and H atoms, respectively.

Vibrational Analysis

In order to have large enough unit cell so that artificial interactions don't affect the forces and consequently the calculated frequencies, we have doubled the unit cell in our vibrational analysis. As such, all the vibrational calculations were done in a $(6 \times 3\sqrt{3})$ rect unit cell. In RAIRS spectroscopy, vibrational modes that lead to an oscillating dipolar moment perpendicular to the surface are active. As such, the relative intensities in the theorical vibrational spectra, as shown in Figure 3, are obtained from the square of the first derivative of the dipole moment normal to the surface with respect to the normal mode (Q_k) as shown in the Equation 7:

$$I_k \propto \left(\frac{\partial \mu_z}{\partial Q_k} \right)^2 \qquad (7)$$

where I_k is the peak intensity and μ_z is the dipole moment in the z direction (which is perpendicular to the surface).[11-15] In first principles-based calculations, these derivates are obtained from derivatives with respect to the motion of the individual nuclei along the x, y and z axis (r_c in general), for the N atoms considered in the frequency calculation, $\partial \mu_z / \partial r_c$. Using the vectors that diagonalize the mass-weighted Hessian matrix, V_{ck}, it is possible to evaluate these derivates with respect to the normal modes:

$$\frac{\partial \mu_z}{\partial Q_k} = \sum_{c=1}^{3N} \frac{V_{ck}}{\sqrt{m_c}} \frac{\partial \mu_z}{\partial r_c} \qquad (8)$$

where m_c is the mass of the atom corresponding to the r_c cartesian displacement. A Lorentzian spreading with is added to the peaks with visual comparison with experimental spectra. An arbitrary width of 20 cm^{-1} applied to combine peaks of similar frequency while maintaining distinctions in peaks of different types. The vibrational modes can be visualized from the additional files that are given in the supplementary information, as detailed below.

Supplemental Movie Index:

Movie 1 (d1cc01574e9.mp4): Visualization of the vibrational mode at 901 cm^{-1} (CH$_2$ wagging). The pink, gray and white spheres are Cu, C and H atoms, respectively.

Movie 2 (d1cc01574e10.mp4): Visualization of the vibrational mode at 989 cm^{-1} (C=CH$_2$ twisting). The pink, gray and white spheres are Cu, C and H atoms, respectively.

Movie 3 (d1cc01574e1.mp4): Visualization of the vibrational mode at 1449 cm^{-1} (CH$_2$ and CH$_3$ scissoring). The pink, gray and white spheres are Cu, C and H atoms, respectively.

Movie 4 (d1cc01574e2.mp4): Visualization of the vibrational mode at 1646 cm^{-1} (C=C symmetric stretching). The pink, gray and white spheres are Cu, C and H atoms, respectively.

Movie 5 (d1cc01574e3.mp4, d1cc01574e4.mp4): Visualization of the vibrational mode at 2919, 2967 cm^{-1} (CH$_3$ symmetric stretching). The pink, gray and white spheres are Cu, C and H atoms, respectively.

Movie 6 (d1cc01574e5.mp4, d1cc01574e6.mp4): Visualization of the vibrational mode at 3012, 3042 cm^{-1} (CH_3 asymmetric stretching). The pink, gray and white spheres are Cu, C and H atoms, respectively.

Movie 7 (d1cc01574e8.mp4, d1cc01574e7.mp4): Visualization of the vibrational mode at 3117, 3109 cm^{-1} (CH_2 asymmetric stretching). The pink, gray and white spheres are Cu, C and H atoms, respectively.

References

1   G. Kresse and J. Furthmüller, *Phys. Rev. B*, 1996, **54**, 11169–11186.

2   G. Kresse and J. Hafner, *Phys. Rev. B*, 1993, **47**, 558–561.

3   G. Kresse and D. Joubert, *Phys. Rev. B*, 1999, **59**, 1758–1775.

4   K. Lejaeghere, G. Bihlmayer, T. Björkman, P. Blaha, S. Blügel, V. Blum, D. Caliste, I. E. Castelli, S. J. Clark, A. Dal Corso, S. De Gironcoli, T. Deutsch, J. K. Dewhurst, I. Di Marco, C. Draxl, M. Dułak, O. Eriksson, J. A. Flores-Livas, K. F. Garrity, L. Genovese, P. Giannozzi, M. Giantomassi, S. Goedecker, X. Gonze, O. Grånäs, E. K. U. Gross, A. Gulans, F. Gygi, D. R. Hamann, P. J. Hasnip, N. A. W. Holzwarth, D. Iuşan, D. B. Jochym, F. Jollet, D. Jones, G. Kresse, K. Koepernik, E. Küçükbenli, Y. O. Kvashnin, I. L. M. Locht, S. Lubeck, M. Marsman, N. Marzari, U. Nitzsche, L. Nordström, T. Ozaki, L. Paulatto, C. J. Pickard, W. Poelmans, M. I. J. Probert, K. Refson, M. Richter, G. M. Rignanese, S. Saha, M. Scheffler, M. Schlipf, K. Schwarz, S. Sharma, F. Tavazza, P. Thunström, A. Tkatchenko, M. Torrent, D. Vanderbilt, M. J. Van Setten, V. Van Speybroeck, J. M. Wills, J. R. Yates, G. X. Zhang and S. Cottenier, *Science*, 2016, **351**, 1415.

5   J. Klimeš, D. R. Bowler and A. Michaelides, *Phys. Rev. B*, 2011, **83**, 195131.

6   J. Klimeš, D. R. Bowler and A. Michaelides, *J. Phys. Condens. Matter*, 2010, **22**, 022201.

7   W. P. Davey, *Phys. Rev.*, 1925, **25**, 753–761.

8   R. T. Hannagan, K. Groden, A. M. Larson, A. J. Therrien, T. Thuening, A. C. Schilling, J.-S. McEwen and E. C. H. Sykes, *Phys. Rev. Res.* 2020, **2**, 023326.

9   S. C. Street and A. J. Gellman, *J. Phys. Chem. B*, 1997, **101**, 1389–1395.

10   B. Hammer, L. B. Hansen and J. K. Nørskov, *Phys. Rev. B*, 1999, **59**, 7413–7421.

11   J. M. Bray, J. L. Smith and W. F. Schneider, *Top. Catal.*, 2014, **57**, 89–105.

12   B. Martorell, A. Clotet and J. Fraxedas, *J. Comput. Chem.*, 2010, **31**, 1842–1852.

13   E. B. W. Jr., J. C. Decius and P. C. Cross, *Molecular Vibrations: The Theory of Infrared and Raman Vibrational Spectra*, Dover Publications, 1980.

14   C. Morin, D. Simon and P. Sautet, *J. Phys. Chem. B*, 2003, **107**, 2995–3002.

15   P. Singnurkar, I. Bako, H. P. Koch, E. Demirci, A. Winkler and R. Schennach, *J. Phys. Chem. C*, 2008, **112**, 14034–14040.